

Mechanical behavior and failure analysis of granite specimens containing two orthogonal fissures under uniaxial compression

Qian Yin^{1,2} · Hongwen Jing¹ · Tantan Zhu¹

Received: 15 January 2015 / Accepted: 10 September 2015 / Published online: 10 December 2015
© Saudi Society for Geosciences 2015

Abstract The mechanical behavior, crack initiation stress, cracking modes, and crack coalescence process due to uniaxial compressive loading for brittle granite specimens ($70 \times 140 \times 29$ mm in size) containing two orthogonal fissures with different “virtual ligament length” were first modeled experimentally. Intact granite specimens present typical axial splitting failure, and the ultimate failure of specimens containing a single fissure results mainly from tensile cracks initiated from the fissure tips. Basically, mechanical parameters of granite specimens containing two orthogonal fissures are lower than the values for intact specimens, and the reduction extent is distinctly related to the virtual ligament length. The uniaxial compressive strength, peak axial strain, Young’s modulus, secant Young’s modulus, and crack initiation stress of granite specimens containing two orthogonal fissures present the same trend with the increasing virtual ligament length, i.e., first decrease and then increase, finally once again decrease. The effect of virtual ligament length on the crack initiation type and ultimate failure modes of granite specimens containing two orthogonal fissures is analyzed. Crack types based on the fissure geometry and crack propagation mechanism are identified, and three different crack initiation types are summarized. The crack coalescence is observed and characterized from tips of pre-existing fissures. Relation between the real-time cracking process and axial stress–strain curves of granite

specimens containing two orthogonal fissures for the entire deformation process is captured, and the corresponding axial stress for crack coalescence is also obtained. Each sharp stress drop in axial stress–strain curves indicates an obvious crack coalescence.

Keywords Brittle granite · Two orthogonal fissures · Virtual ligament length · Mechanical behavior · Crack initiation stress · Crack coalescence

Introduction

Natural rock, as a typical complex geological medium, contains a lot of flaws such as fissures, joints, holes, weak surfaces, and faults, which have significant influence on the strength, deformability, and crack coalescence behavior of rock materials. New cracks are readily initiated at the tips of existing flaws under an applied load (Li et al. 2005; Prudencio and Van Sint Jan 2007; Zhang and Wong 2012; Haeri et al. 2014a), and a series of cracking processes eventually control the overall behavior of the rock. Therefore, study on related mechanical properties and the initiation and propagation of cracks in flawed rock plays a vital role in ensuring stability and security of rock engineering.

Many experimental works have been devoted to study the mechanical behavior, crack initiation, propagation, interaction, and coalescence of the pre-existing fissures in flawed specimens made of various substances, including natural rocks and rock-like materials under compressive loading. Feng et al. (2009) carried out a number of experimental studies to explore the mechanism of multi-crack interaction in limestone specimens with two or three fissures of different geometries under coupled uniaxial compressive stress and chemical solutions with different ionic concentrations and

✉ Qian Yin
Jeryin@foxmail.com

¹ State Key Laboratory for Geomechanics and Deep Underground Engineering, China University of Mining and Technology, Xuzhou 221116, China

² School of Civil, Environmental and Mining Engineering, The University of Western Australia, Perth 6009, Australia

pH values. Wong and Einstein (2009) summarized the effects of the flaw angle, ligament angle and length on the cracking processes, and coalescence patterns of marble specimens containing two open fissures and used a high-speed camera to observe the specimens at a macroscopic scale. Yang et al. (2014b) analyzed the effect of fissure angle on the strength and deformation behaviors of sandstone specimens containing combined flaws, and the ultimate failure mode and crack coalescence behavior were evaluated for the flawed specimens. Nine different crack types were identified based on the geometry and crack coalescence mechanism for combined flaws, and the effect of crack coalescence process on the mechanical behaviors was also investigated by using digital photogrammetry. Yin et al. (2014) studied experimentally the coalescence mechanism between two parallel three-dimensional pre-existing surface cracks in granite specimens under uniaxial compression, and the bridge angles between the two pre-existing cracks varied from 0° to 135° . Zhao et al. (2014) used granite models with dimensions of $100 \times 100 \times 200$ mm and acoustic emission technique to examine the development of fracture around pre-existing cylindrical cavities in brittle rocks, and the results indicated that both tensile and compressive stresses play an important role in the fracture evolution process around cavities in brittle rocks.

As for rock-like materials, Wong et al. (2001) conducted uniaxial compression tests for rock-like materials containing three closed flaws to investigate the crack coalescence and peak strength behaviors of fractured rock. The results showed that the peak strength of the specimens depended on the actual number of pre-existing flaws involved in the coalescence, and the mechanism of crack coalescence depended on the flaw arrangement and the frictional coefficient on the flaw surface. Park and Bobet (2009) carried out a comparison between experimental observations for gypsum specimens loaded in uniaxial compression, with open and closed flaws. From which, three types of cracks including wing cracks, coplanar, and oblique cracks were observed, and eight coalescence types were identified. Janeiro and Einstein (2010) conducted uniaxial compression tests on prismatic gypsum specimens containing either one or two inclusions to experimentally investigate the cracking behavior of brittle heterogeneous materials. Three kinds of materials including PMMA, gypsum, and granite were used by Lee and Jeon (2011) to study the crack initiation, propagation, and coalescence at or near pre-existing open cracks or flaws in a specimen under uniaxial compression, and the flaw geometry in the specimen was a combination of a horizontal flaw and an inclined flaw underneath. Haeri et al. (2014b) experimentally modeled the mechanism of crack propagation and crack coalescence due to compressive loading of brittle substances containing pre-existing cracks by using specially made rock-like specimens from Portland Pozzolana Cement, and the breakage process of the specimens was studied by inserting single and double

flaws with different inclination angles at the center and applying uniaxial compressive stress at both ends of the specimen.

Besides, various numerical methods have been developed and used for the simulation of cracking behavior and fracture coalescence in brittle substances. These numerical methods include the boundary element method (BEM) (Aliabadi and Brebbia 1993), finite element method (FEM) (Trädegård et al. 1998; Bouchard et al. 2003), extended finite element method (XFEM) (Belytschko and Black 1999), discrete element method (DEM) (Vesga et al. 2008; Iturrioz et al. 2009), discontinuous deformation analysis (DDA) (Ning et al. 2011; Zhao et al. 2011), scaled boundary finite element method (SBFEM) (Ooi et al. 2012), and numerical manifold method (NMM) (Wu and Wong 2012, 2013). Several computer codes can also be applied to model the failure mechanism of brittle materials such as rocks, for example, Rock Failure Process Analysis (RFPA^{2D}) code (Wong et al. 2002), FROCK code (Park 2008), and 2D Particle Flow Code (PFC^{2D}) (Lee and Jeon 2011; Yang et al. 2014a).

As it is well known, stress redistribution during the underground excavation generates a multitude of new fissures in rock mass, which are mainly characterized with parallel and cross shapes. Many scholars have studied the mechanical behavior and crack coalescence of rocks containing parallel fissures through both experiments and numerical simulation, and a lot of positive results have been obtained. However, the fracture coalescence behavior for rocks containing cross fissures has rarely been experimentally reported. In this study, a new pre-existing fissure geometry that consisted of a pair of orthogonal fissures was first simplified and introduced according to the induced fissure orientation in the protective coal pillar at tunnel 5937 of Tashan mine in China, as shown in Fig. 1. Uniaxial compression tests for brittle granite specimens containing two orthogonal fissures were conducted by using a rock mechanic servo-controlled testing system, and a high-speed camera was also used to capture the real-time crack coalescence process of the flawed specimens during the loading process. The emphasis on this research was to investigate the influence of the “virtual ligament length” c of the two orthogonal fissures on the mechanical behavior and the crack initiation, propagation, and coalescence process of the flawed granite specimens containing two orthogonal fissures.

Granite material and experimental procedure

Granite material and specimen preparation

In this work, the brittle granite material from Linyi City in the Shandong Province of China, which is widely distributed in the continental crust, was chosen as the test rock. The tested granite, with a crystalline and blocky structure, is a kind of medium-grained heterogeneous material with the average



Fig. 1 A photo that mainly contains simplified orthogonal fissures (in the protective coal pillar at tunnel 5937 of Tashan mine in China)

density of about 2690 kg/m^3 . The granite is porous. Based on the result of X-ray diffraction (XRD) (Fig. 2), the main minerals in the granite specimens are quartz and feldspar, with minor quantities of margarite and gismondine. Moreover, the tested granite has no surface texture visible to naked eye and with the color of gray in natural state.

To investigate the mechanical behavior and crack coalescence evolution of pre-cracked rock, granite specimens containing two orthogonal fissures were prepared to conduct uniaxial compression tests in natural and dry conditions. The specimens were cut from the same rectangular granite block, and when cutting, the specimens were machined along the same direction in the block in order to minimize the influence of anisotropy on the final test results (Yang and Jing 2011).

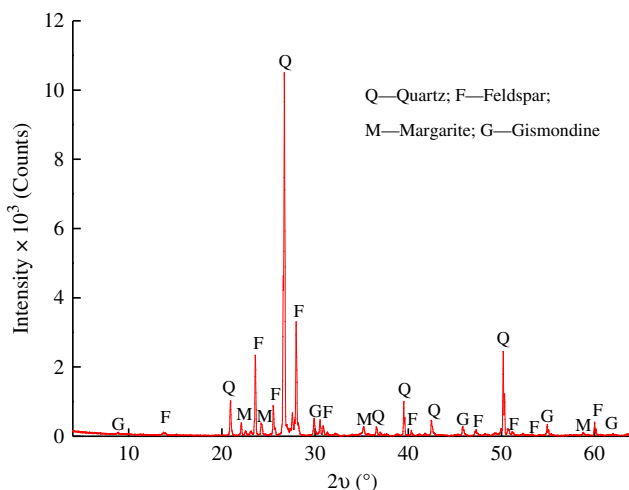


Fig. 2 XRD analysis of the tested granite material in this research

According to the method suggested by the ISRM (Fairhurst and Hudson 1999), all the specimens have a height-to-width ratio of 2.0 to ensure a uniform stress state within the central part of the specimens, and the size of all tested granite specimens is rectangular with 70 mm in width, 140 mm in height, and 29 mm in thickness.

A high-pressure water jet cutting machine (Lee and Jeon 2011; Yang et al. 2014b) was used in this study to cut a pair of orthogonal fissures with the distribution of “T” shape in the intact granite specimens, and the width of all pre-existing fissures was about 1.5 mm. The geometry of the flawed granite specimen containing two orthogonal fissures is described in Fig. 3, and geometric parameters of the fissures in the specimens are defined as follows: $2a$ is the primary fissure length, b is the secondary fissure length, β is the primary fissure angle (the angle of the primary fissure to the horizontal direction), and c is the virtual ligament length (distance between the point of intersection of the two fissures and the upper tip of the primary fissure).

In order to accurately investigate the effect of virtual ligament length c on the mechanical properties and crack coalescence behavior of the flawed granite specimens containing two orthogonal fissures under uniaxial compression, different fissure geometries by varying c while keeping other parameters constant were chosen in this study. A detailed description of the specimens containing two orthogonal fissures is given in Table 1.

Experimental procedure

The uniaxial compression tests for the granite specimens were conducted using a rock mechanic servo-controlled testing system (CSS-55000) with the maximum loading capacity of 500 kN in China University of Mining and Technology. The axial stress was imposed on the surface of the specimen until the ultimate failure took place. Before that, two rigid steel plates, with dimensions of $50 \times 150 \times 20 \text{ mm}$, were placed between the loading frame and the specimen, and a layer of

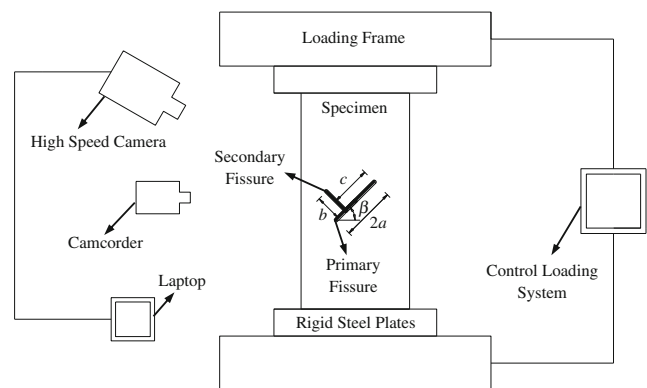


Fig. 3 Geometry of the flawed granite specimen containing two orthogonal fissures and schematic of a typical experimental setup

Table 1 Geometric and mechanical parameters of the granite specimens under uniaxial compression

Specimen	H (mm)	W (mm)	T (mm)	$2a$ (mm)	β (°)	b (mm)	c (mm)	σ_c (MPa)	E (GPa)	E_T (GPa)	ε_{1c} (10^{-2})
1-1	139.53	69.77	29.06	30	45	15	0	79.54	9.40	6.75	1.179
1-2	139.73	69.64	29.09	30	45	15	0	76.31	9.41	6.39	1.194
2-1	139.72	69.81	29.04	30	45	15	7.5	58.84	7.45	5.33	1.103
2-2	139.75	69.97	28.96	30	45	15	7.5	62.13	7.84	5.40	1.151
3-2	139.52	69.69	28.84	30	45	15	15	52.52	6.93	5.01	1.048
3-3	139.82	70.02	29.76	30	45	15	15	48.52	6.91	4.83	1.004
4-1	139.96	69.94	28.92	30	45	15	22.5	69.53	8.42	6.47	1.075
4-2	139.86	69.89	28.87	30	45	15	22.5	66.56	8.73	6.35	1.048
5-1	139.46	69.78	29.28	30	45	15	30	36.03	7.54	4.96	0.727
5-2	139.73	69.81	29.67	30	45	15	30	32.74	7.38	4.87	0.672
6-1	139.73	69.84	28.94	30	45	Specimens containing a single fissure		79.97	9.73	6.94	1.152
6-2	139.66	69.81	28.99	30	45			79.61	9.31	6.78	1.174
7-5	139.81	69.84	28.94	Intact specimens				120.66	10.49	8.32	1.450
7-9	139.57	69.80	28.84					122.92	10.23	7.69	1.599

W width, H height, T thickness

petroleum jelly was evenly coated between the two rigid steel plates and end surfaces of the specimen in order to reduce the end friction effects. All tests were conducted under displacement-controlled conditions with the loading rate of 0.08 mm/min. During the uniaxial compression, the axial loads and deformations of the specimens were recorded simultaneously, and the real-time crack coalescence process was captured with a high-speed camera at the same time. A schematic of the setup is shown in Fig. 3.

Experimental results and discussion

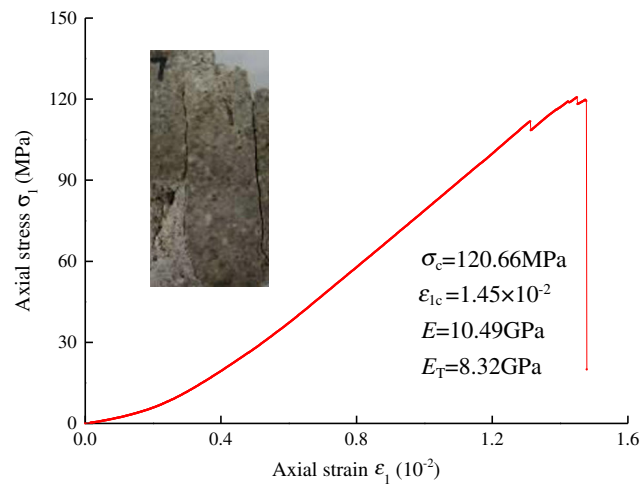
Axial stress–strain curves and the cracking process of the intact and flawed granite specimens containing a single fissure

Figure 4a presents the axial stress–strain curve and the ultimate failure mode of the intact granite specimen no. 7–5 under uniaxial compression, in which the corresponding mechanical parameters are also listed. Here, σ_c refers to the peak strength and the ε_{1c} is defined as the peak axial strain. The Young's modulus E refers to the average slope of the axial stress–strain curve for the tested granite in the elastic stage, and the E_T is the secant Young's modulus from zero stress to its uniaxial compressive strength. It can be seen from Fig. 4a that axial stress of the intact specimen drops abruptly after the peak axial strain, presenting typical brittle characteristics. The ultimate failure mode of the intact granite specimen takes on axial splitting failure. Corresponding cracking process for the entire deformation of the intact specimen is also captured, as shown in Fig. 4b. No cracking can be observed in the intact specimen by unaided eyes before point A ($\sigma_1=111.74$ MPa=91.61 %

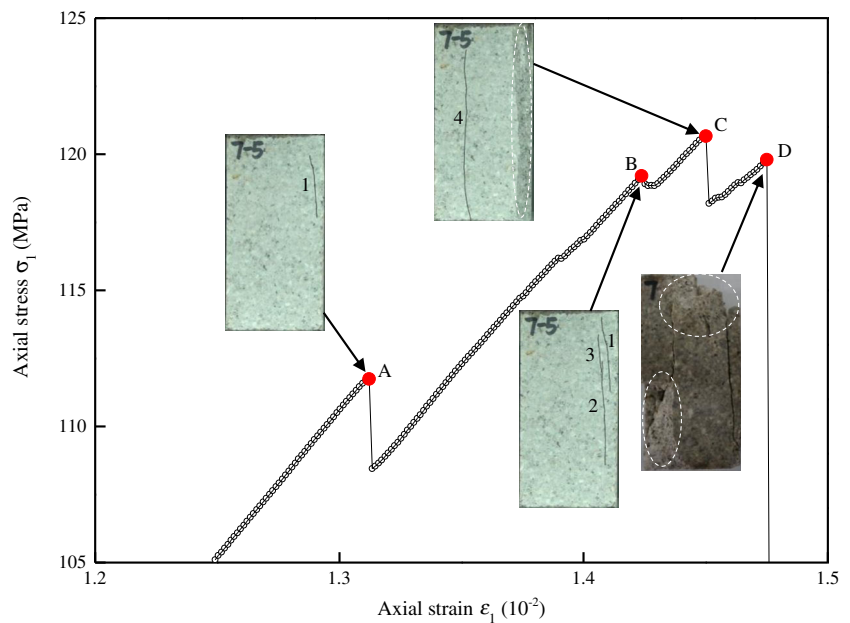
σ_c). However, when the specimen is loaded to point A, crack 1 (vertical splitting tensile failure) first initiates at the upper right corner of the specimen, and propagates rapidly along the direction of axial loading, which leads to the first axial stress drop to 108.45 MPa. Afterward, the axial stress increases gradually with the increasing axial deformation, and when the specimen is loaded to point B ($\sigma_1=119.20$ MPa=98.79 % σ_c), vertical splitting tensile crack 2 and crack 3 initiate near crack 1 at the same time, and quickly propagate, coalescing into one wider crack finally. At this moment, the second stress drop occurs, falling from 119.20 to 118.83 MPa. Continuous increase of the axial deformation causes the specimen to quickly reach the peak stress point C ($\sigma_1=120.66$ MPa=100 % σ_c). During this process, tensile crack 4 forms and evolves rapidly toward both the upper and under specimen boundaries, accompanying with some surface spalling failure at the right side region of the specimen, as shown in the elliptical region of Fig. 4b, leading to the third stress drop from 120.66 to 118.20 MPa. However, after the third stress drop, the axial supporting capacity continues to increase slowly, for the specimen still has a good supporting structure. When the axial stress is loaded to point D ($\sigma_1=119.80$ MPa=99.29 % σ_c), some rapid spalling damage of the specimen can be observed. At this moment, the specimen loses the bearing capacity with a loud failure sound. Ultimate brittle failure occurs quickly, resulting in rapid reduction of the axial stress to 20.79 MPa.

Due to the heterogeneity of rock, it is difficult to obtain completely same experimental results for two different specimens even though with the same testing conditions and specimen scale. Figure 5a shows the effect of heterogeneity on axial stress–strain curves of granite specimens containing a single fissure under uniaxial compression. The figure shows

Fig. 4 Axial stress–strain curve, ultimate failure mode, and the cracking process of the intact granite specimen no. 7–5 under uniaxial compression



(a) Axial stress–strain curve and the ultimate failure mode of the intact specimen 7-5#

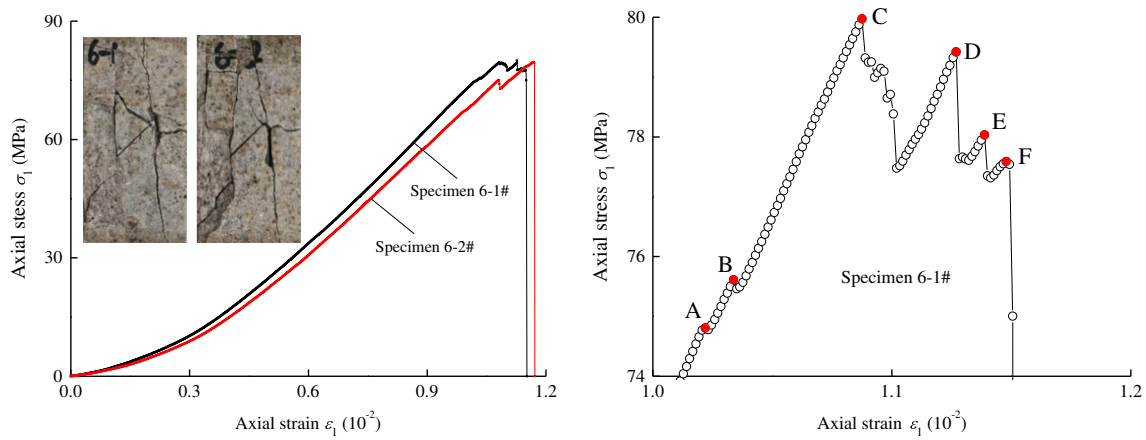


(b) Cracking process of the intact specimen 7-5#

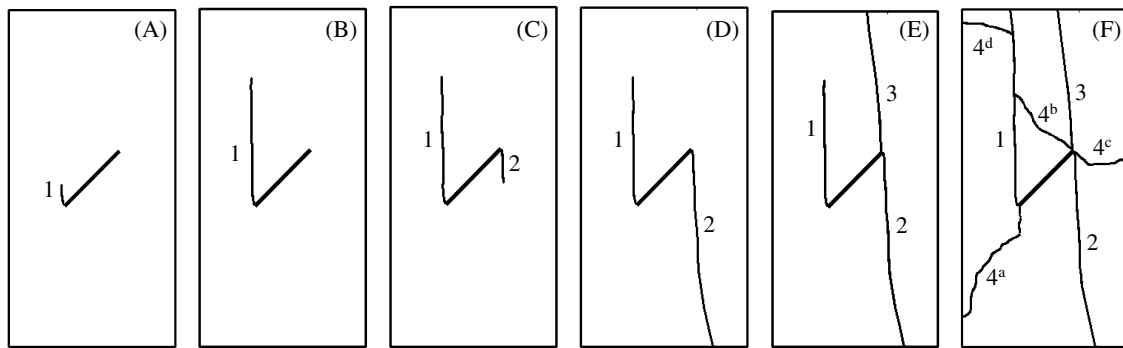
that, for specimens containing a single fissure with the same geometry, the axial stress–strain curves exhibit very good consistency. The peak strengths of specimen nos. 6–1 and 6–2 are 79.97 and 79.61 MPa, respectively, and the discrete coefficient (the ratio of standard deviation to the average value) is 0.23 %. The corresponding peak axial strains are 1.152×10^{-2} and 1.174×10^{-2} , respectively, and the discrete coefficient is 0.96 %. The Young’s moduli are 9.73 and 9.31 GPa, respectively, and the discrete coefficient is 0.22 %. The above analysis indicates that heterogeneity of the tested granite material has a negligible effect on the strength and deformation parameters of the specimens containing a single fissure with the same geometry, and the effect of virtual ligament length on the mechanical behavior and failure mechanism of granite

specimens containing two orthogonal fissures can be accurately studied.

Cracking process of the granite specimen containing a single fissure under uniaxial compression is analyzed for the entire deformation process, as shown in Fig. 5a, b. When the axial stress is loaded to point A ($\sigma_1 = 74.80 \text{ MPa} = 93.53 \% \sigma_c$) and point B ($\sigma_1 = 75.61 \text{ MPa} = 94.55 \% \sigma_c$), initiation and propagation of crack 1 from the lower tip of the pre-existing fissure lead to two slight axial stress drops. Afterward, when the specimen is loaded to the peak strength point C ($\sigma_1 = 79.97 \text{ MPa} = 100 \% \sigma_c$), shear crack 2, which initiates from the upper tip of the fissure, leads to the third stress drop from 79.79 to 77.47 MPa, accompanying with some surface spalling during this process. Then, the crack 2 continues to evolve to the under specimen boundary with the increasing



(a) Axial stress-strain curves



(b) Cracking process of the specimen 6-1# (the denoted letters correspond to those shown in Fig. 5(a))

Fig. 5 Axial stress–strain curves and the cracking process of granite specimens containing a single fissure under uniaxial compression

axial deformation (point D, $\sigma_1=79.42 \text{ MPa}=99.31 \% \sigma_c$), which leads to a stress drop from 79.42 to 77.60 MPa. However, the specimen still has not lost the bearing capacity completely, when the axial stress is loaded to point E ($\sigma_1=78.03 \text{ MPa}=97.57 \% \sigma_c$), initiation and rapid propagation of crack 3 from the upper tip of the fissure lead to a stress drop to 77.31 MPa. When the axial stress continues to increase to point F ($\sigma_1=77.59 \text{ MPa}=97.02 \% \sigma_c$), crack 1 propagates toward the upper specimen boundary and crack 4^a initiates from the lower tip of the fissure. Besides, crack 4^b occurs from the upper tip of the fissure and propagates rapidly to coalesce with the crack 1. At this time, the axial stress drops sharply and the specimen loses the bearing capacity, accompanied by cracks 4^c and 4^d.

Strength and deformation behaviors of granite specimens containing two orthogonal fissures

Figure 6 depicts the axial stress–strain curves of the granite specimens containing two orthogonal fissures with different virtual ligament lengths ($c=0, 7.5, 15, 22.5, \text{ and } 30 \text{ mm}$, respectively). It can be seen that the initial compaction stage of the axial stress–strain curves is obvious, presenting typical

concave shapes, which results mainly from the closure of original fissures and pores in the rock material. After that, the elastic deformation begins to dominate the axial stress–strain curves, and the axial stress has an approximately linear

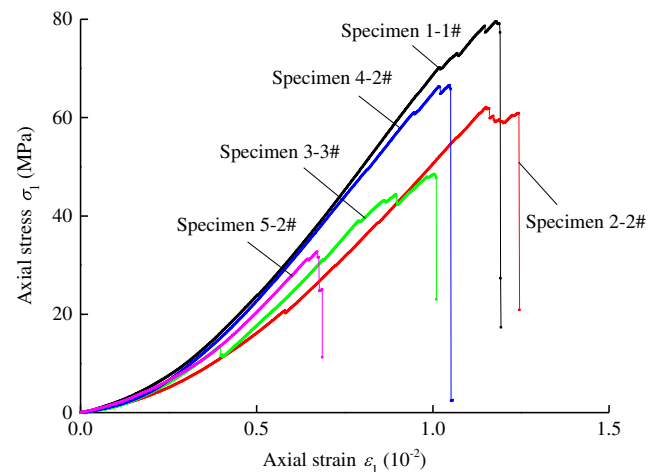


Fig. 6 Axial stress–strain curves of the granite specimens containing two orthogonal fissures with different “virtual ligament lengths” under uniaxial compression

relation with the axial strain. However, with the initiation, propagation, and coalescence of new cracks in the flawed specimens due to axial loading, fluctuations and stress drops are observed in the axial stress–strain curves. After several stress drops, the specimen will reach the maximum axial deformation, at which time the axial stress drops rapidly and the specimen loses the bearing capacity, presenting obvious brittle characteristics.

Figure 7 shows the influence of virtual ligament length c on the strength and deformation properties of granite specimens containing two orthogonal fissures under uniaxial compression, and the relevant mechanical parameters are listed in Table 1. Basically, the mechanical parameters of flawed specimens containing two orthogonal fissures are lower than those for the intact specimens presented in Fig. 4, and the reduction extent has a close relation with the virtual ligament length, which can be summarized as follows. The intact granite

specimens have an average peak strength of 121.79 MPa, while that for the flawed specimens containing two orthogonal fissures ranges from 34.39 MPa ($c=30$ mm) to 77.92 MPa ($c=0$ mm), indicating reductions of 36.02–71.77 % compared with the value of intact specimens. The average peak axial strain for the intact granite specimens is 1.524×10^{-2} , while the flawed specimens have an average peak axial strain of 1.186×10^{-2} ($c=0$ mm), 1.127×10^{-2} ($c=7.5$ mm), 1.026×10^{-2} ($c=15$ mm), 1.061×10^{-2} ($c=22.5$ mm), and 0.699×10^{-2} ($c=30$ mm), showing decreases of 22.18, 26.05, 32.68, 30.38, and 54.13 %, respectively, over the value for intact specimens. The reduction extent of both two Young’s moduli for the flawed granite specimens containing two orthogonal fissures also depend on the virtual ligament length. Taking the Young’s modulus for example, the average E of intact specimens is 10.36 GPa, while that for the flawed specimens containing two orthogonal fissures ranges from 6.92 GPa ($c=$

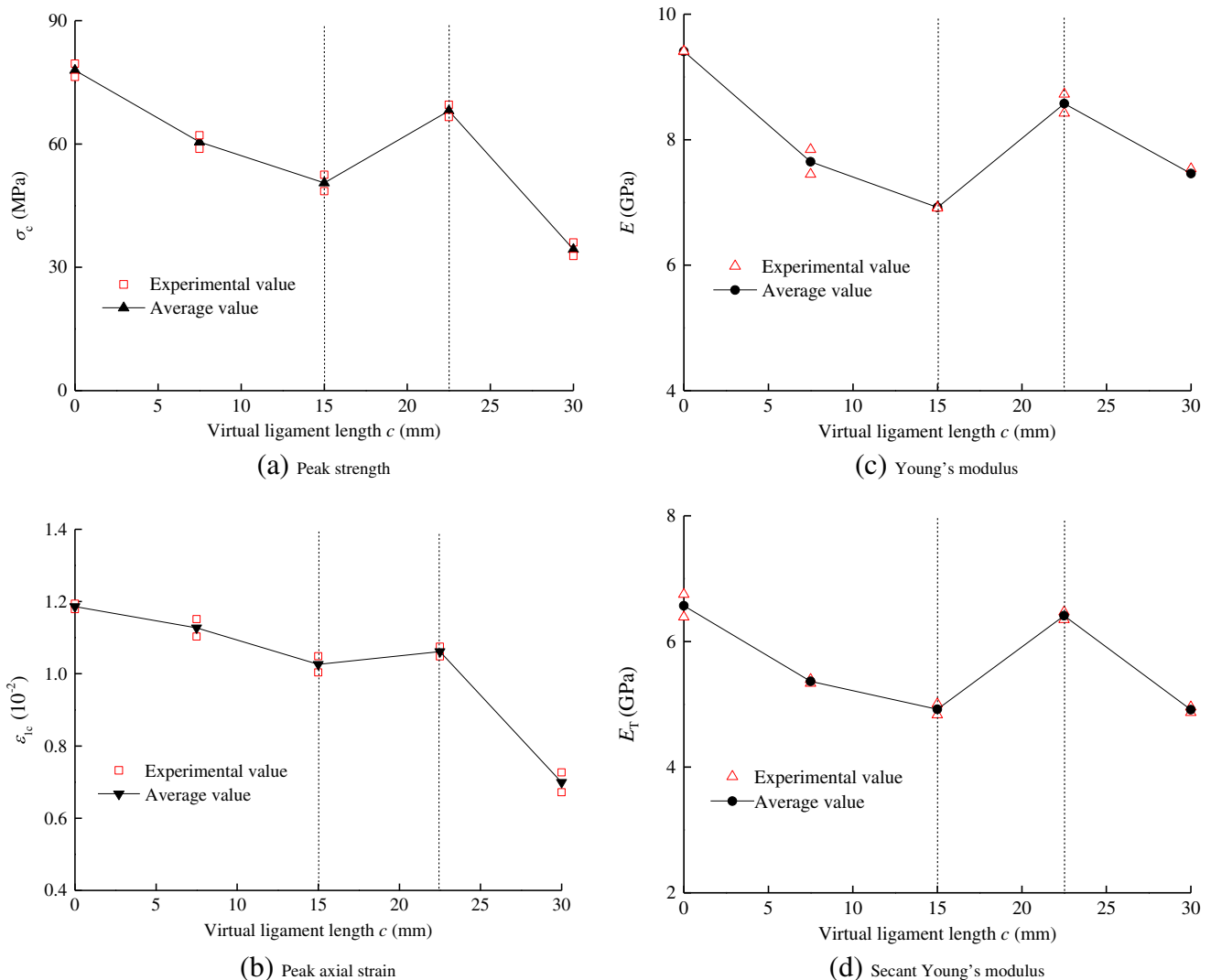


Fig. 7 Influence of “virtual ligament length” c on the strength and deformation parameters of granite specimens containing two orthogonal fissures

15 mm) to 9.41 GPa ($c=0$ mm), with the reduction extent between 9.17 and 33.20 % compared with that for intact specimens.

The effect of virtual ligament length c on the uniaxial compressive strength of flawed granite specimens containing two orthogonal fissures is shown in Fig. 7a. The σ_c first decreases, then increases, and finally once again decreases with the increasing virtual ligament length. The average σ_c at $c=0$ mm is 77.92 MPa, while it decreases to 50.52 MPa when c increases to 15 mm, decreasing by 35.17 % compared with that for $c=0$ mm. As c increases from 15 to 22.5 mm, the average σ_c for granite specimens containing two orthogonal fissures increases from 50.52 to 68.04 MPa, by 34.68 %. Whereas when c is increased from 22.5 to 30 mm, the average σ_c once again decreases, from 68.04 to 34.39 MPa, showing a decrease of 49.46 %.

Figure 7b displays the effect of virtual ligament length on the peak axial strain of granite specimens containing two orthogonal fissures under uniaxial compression, which is similar to the variance on the peak strength (see Fig. 7a). The average peak axial strain of specimens containing two orthogonal fissures with $c=0$ mm is approximately 1.186×10^{-2} , while that for $c=15$ mm is 1.076×10^{-2} , decreasing by 9.27 % compared with the value for $c=0$ mm. In general, the peak axial strain of specimens containing two orthogonal fissures has a little increase from 1.076 to 1.111×10^{-2} with the increase of c from 15 to 22.5 mm. However, when the c increases from 22.5 to 30 mm, the average ε_{1c} of flawed specimens decreases rapidly from 1.111 to 0.699×10^{-2} , by 37.07 %.

In accordance with Fig. 7c, d, the influence of virtual ligament length on the Young's modulus and secant Young's modulus for granite specimens containing two orthogonal fissures under uniaxial compression can be analyzed, respectively. It is very clear that both the two Young's moduli all depend on the virtual ligament length, and the relationship is qualitatively similar to those for the uniaxial compressive strength and peak axial strain. Both Young's moduli decrease in the range of c from 0 to 15 mm, then increase from 15 to 22.5 mm, and finally once again decrease from 22.5 to 30 mm. Taking the Young's modulus for example, the average E decreases from 9.41 to 6.92 GPa, by 26.46 %, with the increasing c from 0 to 15 mm, and then, it increases to 8.57 GPa at $c=22.5$ mm. Finally, as c increased from 22.5 to 30 mm, the average E decreases once again from 8.57 to 7.46 GPa, by 12.95 %.

Cracking mode analysis

According to the nine different crack types identified based on the fissure geometry and crack propagation mechanisms (tensile crack, shear crack, lateral crack, far-field crack, and surface spalling) by Yang et al. (2014b), cracking modes of the brittle granite specimens containing two orthogonal fissures with different virtual ligament lengths can be analyzed, as

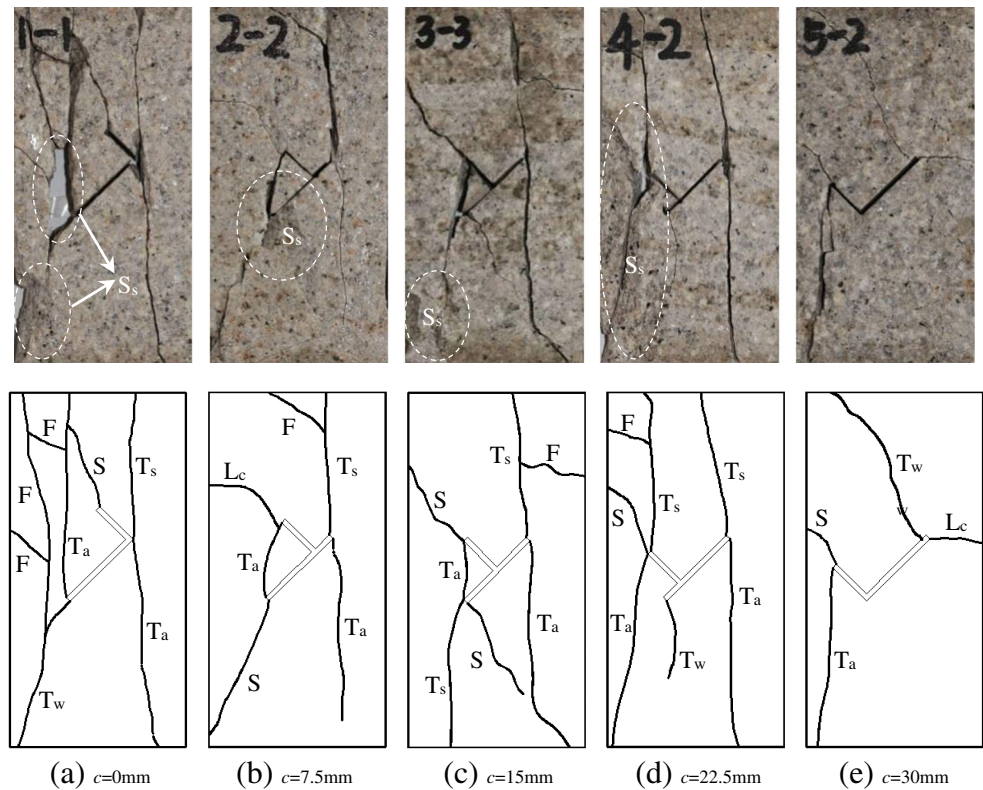
shown in Fig. 8. Crack types in those flawed specimens are listed in Table 2. It can be seen that cracking modes of the granite specimens containing two orthogonal fissures are significantly different with those for the flawed specimens containing a single fissure presented in Fig. 5, and the crack coalescence patterns for specimens containing two orthogonal fissures are different with respect to the virtual ligament length c .

For $c=0$ mm, two tensile cracks, including one anti-tensile crack and one secondary tensile crack, are observed initiating from the upper tip of the primary fissure, and propagating toward the specimen boundaries, which generate one failure plane in the ultimate failure mode of the specimen, as shown in Fig. 8a. Besides, one shear crack, which occurs from the outer tip of the secondary fissure, finally coalesces with the anti-tensile crack initiated from the lower tip of the primary fissure. One tensile wing crack, which initiates from the lower tip of the primary fissure and propagates toward the under specimen boundary, forms another failure plane in the specimen. Note that the propagation path of the tensile crack is not perfectly parallel to the major principal stress direction, but very tortuous through the specimen, which is probably due to the fact that the crack always propagates along the boundaries of large mineral grains within the granite matrix. Moreover, several far-field cracks are also observed, accompanied by some surface spalling in the left side region of the specimen during the loading process.

When c is 7.5 and 15 mm, the cracking modes, which are various with that for $c=0$ mm, are very similar in the two specimen nos. 2–2 and 3–3 even though with some minor differences. Two tensile cracks initiate from the upper tip of the primary fissure and propagate toward the specimen boundaries, producing a failure plane in both the two specimens. There is all one anti-tensile crack, which emanates in the region between the lower tip of the primary fissure and the outer tip of the secondary fissure, connecting these two flaws together and forming a free-standing “triangular prism structure” within the two specimens. One lateral crack while one shear crack is observed initiating from the outer tip of the secondary fissure in specimen nos. 2–2 and 3–3, respectively. However, for cracks initiated from the lower tip of the primary fissure, the cracking mode also differs in the two specimens. In specimen no. 2–2, one shear crack occurs and propagates toward the under specimen boundary. Whereas in specimen no. 3–3, apart from one shear crack, one secondary tensile crack is also observed initiating and propagating along the axial stress direction.

For $c=22.5$ mm, there are also two tensile cracks emanating from the upper tip of the primary fissure along the axial loading direction, as shown in Fig. 8d, forming a failure plane in the ultimate failure mode of the specimen, which is similar to those for $c=0$, 7.5, and 15 mm. One tensile wing crack initiates from the lower tip of the primary fissure, while the length and aperture thickness of this crack keep basically

Fig. 8 Ultimate failure modes of the granite specimens containing two orthogonal fissures with different “virtual ligament lengths” under uniaxial compression (T_w =tensile wing crack, T_s =secondary tensile crack, T_a =anti-tensile crack, F =far-field crack, L_c =lateral crack, S =shear crack, and S_s =surface spalling)



constant for the entire deformation process, presenting a different pattern compared with those in flawed specimen nos. 1–1, 2–2, and 3–3. Besides, for cracks initiated from the outer tip of the secondary fissure, apart from one shear crack, two tensile cracks are also observed initiating and propagating toward the specimen boundaries, generating another failure plane in the specimen. No crack occurs in the region between the outer tip of the secondary fissure and the lower tip of the primary fissure, and the surface spalling failure is more severe.

Table 2 Crack types of the granite specimens containing two orthogonal fissures with different “virtual ligament length” c under uniaxial compression

c (mm)	Crack types						
	T_w	T_s	T_a	F	S_s	L_c	S
0	√	√	√1	√	√		√
7.5		√	√1	√	√	√	√
15		√	√1	√	√		√
22.5	√	√	√1	√	√	√	
30	√1		√1			√	√

√1 indicates the first crack which initiates from the tips of the pre-existing fissures

T_w tensile wing crack, T_s secondary tensile crack, T_a anti-tensile crack, F far-field crack, S_s surface spalling, L_c lateral crack, S shear crack

The cracking mode in the specimen for $c=30$ mm (Fig. 8e) is obviously different with those for the flawed specimens with the virtual ligament length c of 0, 7.5, 15, and 22.5 mm. One tensile wing crack initiates from the upper tip of the primary fissure, first propagating along the direction vertical to the primary fissure, then gradually departing toward the axial loading direction, and finally along an obliquely upward direction mainly resulting from heterogeneity of rock and end effects. Besides, one lateral crack is also observed initiating from the upper tip of the primary fissure along the direction vertical to the major principal stress direction. Moreover, one anti-tensile crack from the outer tip of the secondary fissure propagates rapidly toward the under specimen boundary. Generally, crack types and the ultimate failure mode are relatively simple with almost no surface spalling and no cracks initiating from the lower tip of the primary fissure during the whole process.

It needs to be noted that the initiation and propagation of new cracks in rock reflect the accumulation and transformation of energy. During the loading process, axial stress imposed by the loading frame actually does work on the specimens, and the work is considered to totally transform into the energy absorbed by the specimens neglecting the energy dissipation. The higher the strength of the rock, the more energy it can accumulate, and more fracture surfaces will be generated to release the energy when deformation failure happens. From Fig. 8, generally, the number of cracks formed in the

specimens containing two orthogonal fissures decreases in the range of c from 0 to 15 mm, then increases as c from 15 to 22.5 mm, and finally decreases once again for $c=30$ mm. Besides, the surface spalling degree presents similar variation, weakening gradually with the increasing c from 0 to 15 mm, then becoming serious for $c=22.5$ mm, and finally with almost no surface spalling when c is 30 mm. The analysis is consistent with the variance on the mechanical parameters for flawed granite specimens containing two orthogonal fissures, with the increasing virtual ligament length under uniaxial compression, as discussed in “Strength and deformation behaviors of granite specimens containing two orthogonal fissures” section.

Crack initiation type and crack initiation stress level

Granite, as a typical kind of heterogeneous material, contains massive flaws such as joints, holes, and weak surfaces, which make it easier to generate a local stress concentration phenomenon during the loading process, and new cracks will be induced when the local concentration stress exceeds the bearing capacity of the rock. Crack initiation stress level is an important index evaluating the heterogeneity of rock materials, which can be defined as follows (Martin 1993, 1997; Wang et al. 2014):

$$K = \frac{\sigma_{c1}}{\sigma_c} \quad (1)$$

in which K is the crack initiation stress level of the rock and σ_c and σ_{c1} are the peak strength and corresponding crack initiation stress of an identical specimen, respectively. However, what needs to be explained is that the judgment criteria for crack initiation stress have not been unified by scholars. Lee and Jeon (2011) and Yang et al. (2011) defined the crack initiation stress as the axial stress when the first macroscopic crack was observed with naked eyes, and in this paper, this empirical definition is referenced to analyze the crack initiation stress variation characteristics of the granite specimens containing two orthogonal fissures with different virtual ligament lengths under uniaxial compression, as shown in Fig. 9. It can be seen that both the crack initiation stress and crack initiation stress level first decrease, then increase, and finally once again decrease with the increasing virtual ligament length, with the turning points at $c=15$ and 22.5 mm, respectively, which is similar to the effect of virtual ligament length on the mechanical parameters of granite specimens containing two orthogonal fissures under uniaxial compression discussed above. For $c=0$ mm, the crack initiation stress and crack initiation stress level are 64.84 MPa and 0.81, respectively, while those two parameters decline to 13.55 MPa and 0.28, respectively, when the virtual ligament length is 15 mm, decreasing by 79.10 and 65.43 %, respectively.

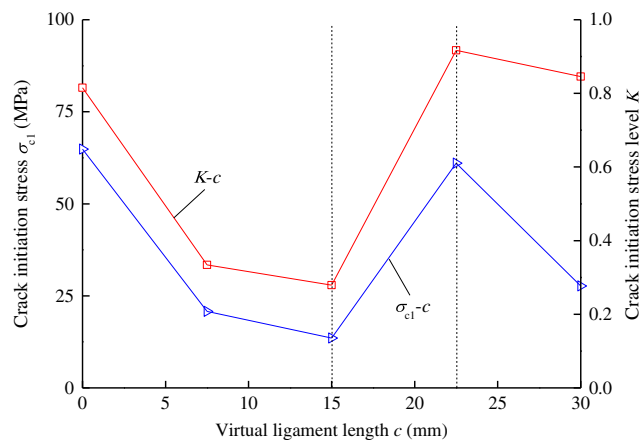


Fig. 9 Effect of “virtual ligament length” c on the crack initiation stress and crack initiation stress level of granite specimens containing two orthogonal fissures under uniaxial compression

Then, the crack initiation stress increases to 61.04 MPa, and the crack initiation stress level increases to 0.92 with the virtual ligament length c of 22.5 mm, which are 3.50 times and 2.28 times larger than the values for $c=15$ mm, respectively. However, both the two parameters once again decrease with the increasing virtual ligament length from 22.5 to 30 mm, showing decreases of 54.66 and 7.82 %, respectively.

Figure 10 and Table 2 plot the crack initiation types of the flawed granite specimens containing two orthogonal fissures with different virtual ligament lengths under uniaxial compression. For $c=0$ and 7.5 mm, one tensile crack first initiates from the lower tip of the primary fissure, propagating along the axial loading direction for $c=0$ mm, while along the direction evolving toward the outer tip of the secondary fissure for $c=7.5$ mm. Figure 10c, d indicate that for flawed specimens with relatively larger virtual ligament lengths of 15 and 22.5 mm, one tensile crack is first observed initiating from the outer tip of the secondary fissure along the direction of axial stress for $c=15$ mm, while along the direction with a certain deviation to the axial stress for $c=22.5$ mm. However, for $c=30$ mm (Fig. 10e), cracks first occur from the upper tip of the primary fissure along the direction approximately vertical to the primary fissure and from the outer tip of the secondary fissure along the major principal stress direction at the same time, respectively.

Real-time crack coalescence process

According to the photographic monitoring results, the relationship between the typical real-time cracking process and axial stress–strain curves of flawed granite specimens containing two orthogonal fissures with different virtual ligament length can be analyzed in detail as follows.

Figure 11 presents the real-time crack coalescence process of the granite specimen containing two orthogonal fissures

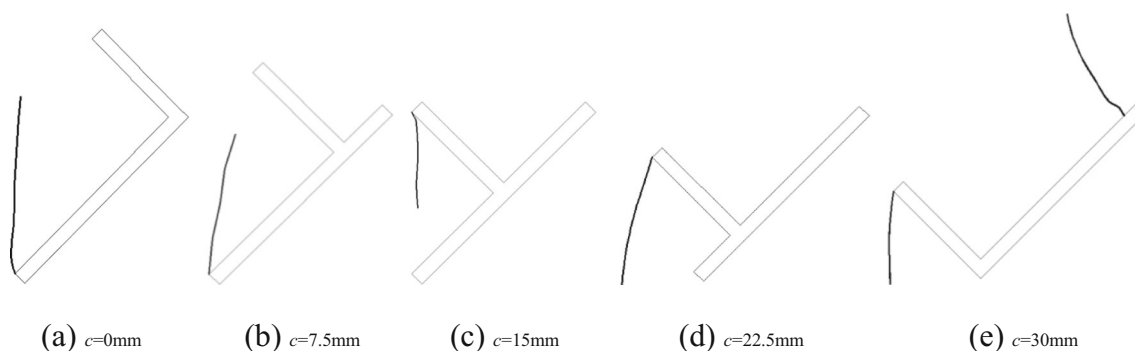
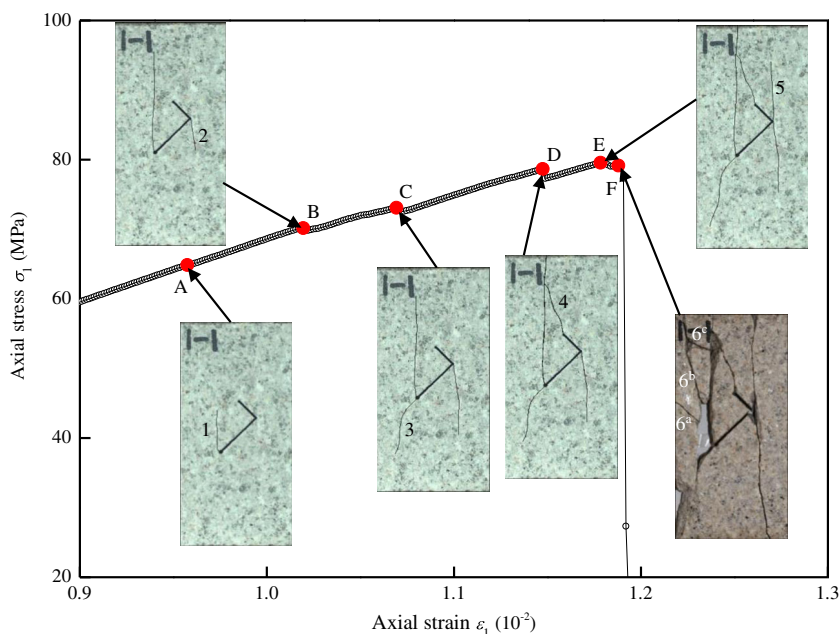


Fig. 10 Crack initiation types of the flawed granite specimens containing two orthogonal fissures with different “virtual ligament lengths” under uniaxial compression

with the virtual ligament length c of 0 mm under uniaxial compression. Before point A ($\sigma_1=64.84 \text{ MPa}=81.52 \% \sigma_c$), the stress concentration nearby the pre-existing fissures does not reach the material strength to initiate any cracks. But when the axial stress is loaded to point A, anti-tensile crack 1 first initiates from the lower tip of the primary fissure and propagates along the direction of axial stress, which leads to slight fluctuations to the axial stress–strain curve. After point A, the axial stress increases gradually with the increasing axial deformation, and when the axial stress is loaded to point B ($\sigma_1=70.16 \text{ MPa}=88.21 \% \sigma_c$), the specimen undergoes the first axial stress drop from 70.16 to 69.86 MPa due to the propagation of tensile crack 1 and initiation of tensile crack 2 from the upper tip of the primary fissure. When the specimen is loaded to point C ($\sigma_1=73.09 \text{ MPa}=91.90 \% \sigma_c$), tensile wing crack 3 initiates from the lower tip of the primary fissure, first along the primary fissure direction, then gradually turning toward the major principal stress direction, and the crack 2

continues to evolve, which leads to the second axial stress drop from 73.09 to 72.52 MPa. When the axial stress is increased to point D ($\sigma_1=78.63 \text{ MPa}=98.86 \% \sigma_c$), crack 1 propagates toward the upper specimen boundary, and shear crack 4 occurs from the outer tip of the secondary fissure, and evolves rapidly to coalesce with the crack 1, resulting in another axial stress drop from 78.63 to 77.31 MPa. However, after undergoing the first three axial stress drops, the specimen still has a good supporting structure. The continuous increase of the axial deformation results in that the specimen is loaded to the peak strength point E ($\sigma_1=79.53 \text{ MPa}=100 \% \sigma_c$). At this time, the specimen begins to produce rapidly the tensile crack 5 from the upper tip of the primary fissure, resulting in the axial stress falling to 79.26 MPa. Afterward, when the axial stress is reduced to point F ($\sigma_1=79.15 \text{ MPa}=99.52 \% \sigma_c$) after the peak strength, all the cracks 2, 3, and 5 propagate toward the specimen boundaries, and the specimen loses the bearing capacity with a loud failure sound. Brittle failure

Fig. 11 Relation between the real-time cracking process and the axial stress–strain curve of the granite specimen containing two orthogonal fissures (specimen no. 1–1, $c=0 \text{ mm}$) under uniaxial compression



occurs quickly, and far-field cracks 6^a , 6^b , and 6^c initiate, which result in a rapid reduction of the axial stress to 17.32 MPa, accompanied by some surface spalling failure during the process.

In accordance with Fig. 12, the real-time cracking process for the granite specimen containing two orthogonal fissures with the virtual ligament length c of 15 mm is analyzed. It can be seen that when the axial stress is loaded to point A ($\sigma_1 = 13.55 \text{ MPa} = 27.94 \% \sigma_c$), anti-tensile crack 1, which initiates from the outer tip of the secondary fissure and evolves to the lower tip of the primary fissure, leads to a small axial stress drop to 11.53 MPa. After the first axial stress drop, the axial stress begins to increase linearly as the increased axial deformation with the Young's modulus of 6.91 GPa. When the axial stress is increased to point B ($\sigma_1 = 31.13 \text{ MPa} = 64.17 \% \sigma_c$), tensile crack 2, which also initiates from the outer tip of the secondary fissure, results in slight fluctuations to the axial stress–strain curve. Afterward, when the axial stress is loaded to point C ($\sigma_1 = 39.00 \text{ MPa} = 80.38 \% \sigma_c$), tensile crack 1 quickly coalesces with the lower tip of the primary fissure, and runs through the whole thickness of the specimen, generating a triangular prism structure with no longer bearing capacity; moreover, secondary tensile crack 3 initiates from the upper tip of the primary fissure. The axial stress drops to 38.81 MPa. With the increasing axial deformation, the axial stress continues to increase to point D ($\sigma_1 = 43.16 \text{ MPa} = 88.96 \% \sigma_c$). At this time, crack 2, similar to tensile crack 1, also propagates toward the lower tip of the primary fissure, and the axial stress undergoes another drop due to the propagation of crack 3 and initiation of tensile wing crack 4 from the lower tip of the primary fissure. When the specimen is loaded

to point E ($\sigma_1 = 44.39 \text{ MPa} = 91.45 \% \sigma_c$), crack 4 evolves rapidly toward the bottom edge of the specimen, and anti-tensile crack 5 initiates from the upper tip of the primary fissure along the major principal stress direction, which results in an axial stress drop to 42.33 MPa. However, when the specimen is loaded to the peak strength point F ($\sigma_1 = 48.52 \text{ MPa} = 100 \% \sigma_c$), both cracks 3 and 5 propagate toward the upper and under specimen boundaries, respectively. After the peak axial stress, brittle failure happens and the axial stress drops abruptly to 23.11 MPa in additional cracks (e.g., shear cracks 6^a and 6^c and far-field crack 6^b).

The real-time cracking process of the granite specimen containing two orthogonal fissures with the virtual ligament length c of 30 mm, as shown in Fig. 13, is significantly different with those for $c=0$ and 15 mm. Anti-tensile crack 1^a first initiates from the outer tip of the secondary fissure along the major principal stress direction; meanwhile, tensile wing crack 1^b occurs from the upper tip of the primary fissure along the direction approximately vertical to the primary fissure when the axial stress is loaded to point A ($\sigma_1 = 27.68 \text{ MPa} = 84.54 \% \sigma_c$), which leads to slight fluctuations to the axial stress–strain curve. Afterward, both cracks 1^a and 1^b continue to widen and lengthen with the increasing axial deformation, while the propagation direction of crack 1^b gradually turns toward the axial loading direction, and finally once again changes the direction with some deviation to the principal stress direction mainly resulting from the heterogeneity of rock and end effects. When the axial stress increases to point B ($\sigma_1 = 31.27 \text{ MPa} = 95.50 \% \sigma_c$), tensile crack 2 initiates from the outer tip of the secondary fissure, leading to an axial stress drop from 31.27 to 31.01 MPa. When the specimen is loaded

Fig. 12 Relation between the real-time cracking process and the axial stress–strain curve of the granite specimen containing two orthogonal fissures (specimen no. 3–3, $c=15$ mm) under uniaxial compression

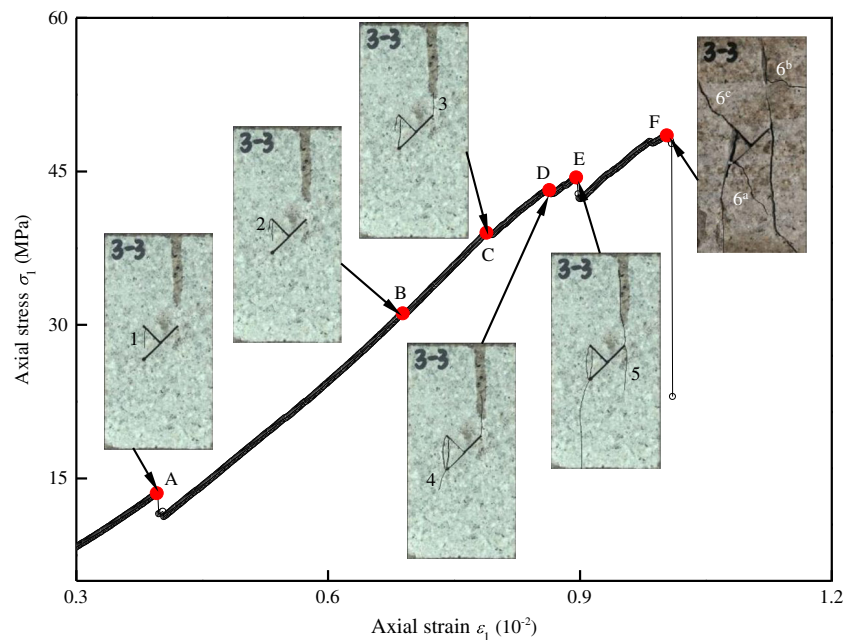
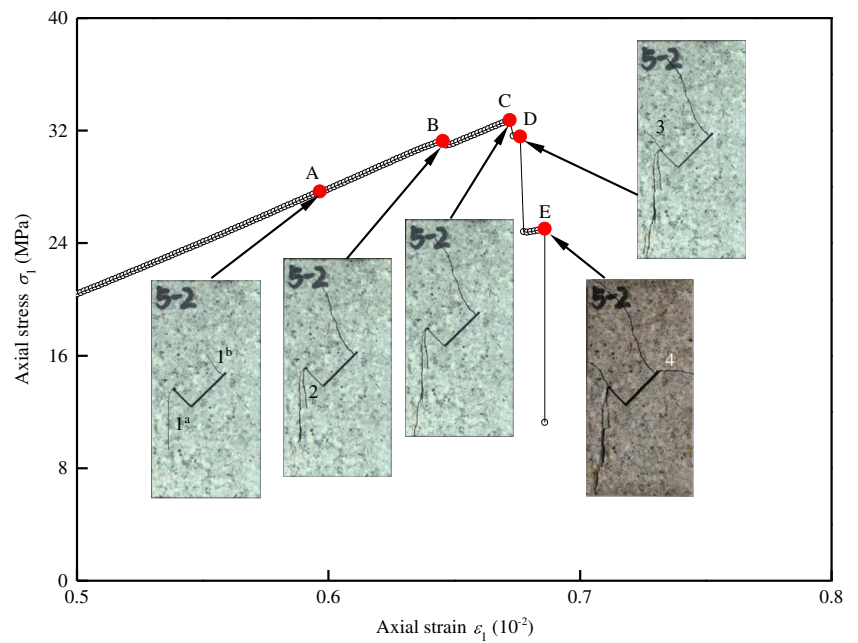


Fig. 13 Relation between the real-time cracking process and the axial stress–strain curve of the granite specimen containing two orthogonal fissures (specimen no. 5–2, $c=30$ mm) under uniaxial compression



to the peak strength point C ($\sigma_1=32.74$ MPa=100 % σ_c), crack 1^b continues to lengthen and crack 1^a evolves toward the under specimen boundary. The axial stress drops to 31.58 MPa. Then, when the axial stress continues to drop to point D ($\sigma_1=31.57$ MPa=96.44 % σ_c) after the peak strength, shear crack 3 initiates from the outer tip of the secondary fissure along the secondary fissure direction, which leads to an abrupt axial stress drop to 24.77 MPa, reducing by 6.80 MPa. However, the specimen has not lost the whole bearing capacity. When the axial stress is loaded to point E ($\sigma_1=25.02$ MPa=76.42 % σ_c), both cracks 1^b and 3 extend toward the boundaries of the specimen. At this time, the specimen loses the bearing capacity with a rapid reduction of the axial stress to 11.25 MPa, accompanying with the lateral crack 4.

Conclusions

The emphasis of this experimental investigation is to explore the strength, deformation failure, cracking modes, and crack coalescence behavior of brittle granite specimens, with dimensions of $70 \times 140 \times 29$ mm, containing a pair of orthogonal fissures (a kind of new fissure geometry) with different virtual ligament lengths of 0, 7.5, 15, 22.5, and 30 mm, respectively, under uniaxial compression. The fissures in the tested granite specimens were all cut by using a high-pressure water jet cutting machine with a fixed water pressure to ensure the machined open fissures with a uniform aperture thickness of

about 1.5 mm. Based on our study, the main conclusions can be drawn as follows:

1. Basically, the mechanical parameters of the flawed granite specimens containing two orthogonal fissures are weaker, showing reductions of 36.02–71.77, 22.18–54.13, 9.17–33.20, and 17.93–38.61 % for the uniaxial compressive strength, peak axial strain, Young’s modulus, and secant Young’s modulus, respectively, compared with the values for intact specimens; moreover, the reduction extent is closely related to the virtual ligament length. The average peak strength of granite specimens containing two orthogonal fissures is decreased from 77.92 to 50.52 MPa as c from 0 to 15 mm, then increased from 50.52 to 68.04 MPa as c from 15 to 22.5 mm, and finally declined once again from 68.04 to 34.39 MPa with the increasing c from 22.5 to 30 mm. The average peak strain for granite specimens containing two orthogonal fissures is first decreased from 1.186 to 1.026×10^{-2} as c from 0 to 15 mm, then increased from 1.026 to 1.061×10^{-2} with c from 15 to 22.5 mm, and finally declined to 0.699×10^{-2} for $c=30$ mm. Both Young’s moduli decrease in the range of c from 0 to 15 mm, then increase in the range of c from 15 to 22.5 mm, and finally decrease up to 30 mm. The average secant Young’s modulus decreases from 6.57 GPa ($c=0$ mm) to 4.92 GPa ($c=15$ mm), then increases to 6.41 GPa ($c=22.5$ mm), and finally decreases from 6.41 GPa ($c=22.5$ mm) to 4.91 GPa ($c=30$ mm).
2. The influence of the virtual ligament length on the crack initiation stress, crack initiation stress level, and the crack initiation type of granite specimens containing two

orthogonal fissures is discussed. Both the crack initiation stress and crack initiation stress level decrease in the range of c from 0 to 15 mm, then increase as c from 15 to 22.5 mm, and finally decrease with the increasing c from 22.5 to 30 mm, presenting similar variation regulation to the mechanical parameters for the specimens containing two orthogonal fissures with the virtual ligament length. With the increasing c from 0 to 15 mm, the crack initiation stress decreases from 64.84 to 13.55 MPa, with the corresponding crack initiation stress level decreasing from 0.82 to 0.28. When the c is increased to 22.5 mm, the crack initiation stress increases to 61.04 MPa, and the corresponding crack initiation stress level increases to 0.92. Finally, the crack initiation stress and crack initiation stress level decrease to 27.68 and 0.85 MPa, respectively, with the virtual ligament length of 30 mm. The crack initiation mode of granite specimens containing two orthogonal fissures under uniaxial compression also depends on the virtual ligament length. For $c=0$ and 7.5 mm, the crack first emanates from the lower tip of the primary fissure, with no cracks initiating from the outer tip of the secondary fissure. For $c=15$ and 22.5 mm, the crack first occurs from the outer tip of the secondary fissure, while no cracks is initiated from the tips of the primary fissure. However, for $c=30$ mm, crack 1^a initiates from the outer tip of the secondary fissure and crack 1^b initiates from the upper tip of the primary fissure, respectively.

- As a typical kind of brittle rock, intact granite specimens present splitting tensile failure under uniaxial compression. Cracking process and the ultimate failure mode of two granite specimens containing a single fissure with the same geometry under uniaxial compression are similar, with the failure planes generated by tensile cracks initiated from the fissure tips. The cracking process for granite specimens containing two orthogonal fissures differs with the virtual ligament length. For $c=0$ mm, the shear crack from the outer tip of the secondary fissure rapidly coalesces with the tensile crack initiated from the lower tip of the primary fissure. For $c=7.5$ and 15 mm, there is all one coalesced crack between the outer tip of the secondary fissure and the lower tip of the primary fissure, forming a free-standing triangular prism structure within the specimens. For $c=22.5$ mm, tensile cracks initiated from the upper tip of the primary fissure and the outer tip of the secondary fissure generate two main tensile failure planes in the specimen. However, for $c=30$ mm, the cracking process is relatively simple, cracks initiated from the outer tip of the secondary fissure, and the upper tip of the primary fissure lead to ultimate failure of the specimen, with no coalesced cracks between the outer tip of the secondary fissure and the upper tip of the primary fissure. According to the photographic monitoring results,

relation between the real-time cracking process and axial stress–strain curves of the specimens containing two orthogonal fissures is captured and discussed, and the corresponding axial stress for crack coalescence is also obtained. Each sharp stress drop in axial stress–strain curves indicates an obvious crack coalescence.

Acknowledgments This work was supported by the State Key Development Program for Basic Research of China (2013CB036003), the Chinese Natural Science Foundation (51374198), and the China Scholarship Council.

References

- Aliabadi MH, Brebbia CA (1993) Advances in boundary element methods for fracture mechanics. Computational Mechanics Publications, Amsterdam
- Belytschko T, Black T (1999) Elastic crack growth in finite elements with minimal remeshing. *Int J Numer Methods Eng* 45(5):601–620
- Bouchard PO, Bay F, Chastel Y (2003) Numerical modelling of crack propagation: automatic remeshing and comparison of different criteria. *Comput Methods Appl Mech Eng* 192(35–36):3887–3908
- Fairhurst CE, Hudson JA (1999) Draft ISRM suggested method for the complete stress–strain curve for intact rock in uniaxial compression. *Int J Rock Mech Min Sc* 36(3):279–289
- Feng XT, Ding WX, Zhang DX (2009) Multi-crack interaction in limestone subject to stress and flow of chemical solutions. *Int J Rock Mech Min Sci* 46(1):159–171
- Haeri H, Shahriar K, Marji MF, Moarefvand P (2014a) On the crack propagation analysis of rock like Brazilian disc specimens containing cracks under compressive line loading. *Latin Am J Solids Struct* 11(8):1400–1416
- Haeri H, Shahriar K, Marji MF, Moarefvand P (2014b) Cracks coalescence mechanism and cracks propagation paths in rock-like specimens containing pre-existing random cracks under compression. *J Cent South Univ* 21(6):2404–2414
- Iturrioz I, Miguel LFF, Riera JD (2009) Dynamic fracture analysis of concrete or rock plates by means of the discrete element method. *Latin Am J Solids Struct* 6(3):229–245
- Janeiro RP, Einstein HH (2010) Experimental study of the cracking behavior of specimens containing inclusions (under uniaxial compression). *Int J Fract* 164(1):83–102
- Lee H, Jeon S (2011) An experimental and numerical study of fracture coalescence in pre-cracked specimens under uniaxial compression. *Int J Solids Struct* 48(6):979–999
- Li YP, Chen LZ, Wang YH (2005) Experimental research on pre-cracked marble under compression. *Int J Solids Struct* 42(9–10):2505–2516
- Martin CD (1993) The strength of massive Lac du Bonnet granite around underground opening. University of Manitoba, Dissertation
- Martin CD (1997) Seventeenth Canadian Geotechnical Colloquium: the effect of cohesion loss and stress path on brittle rock strength. *Can Geotech J* 34(5):698–725
- Ning YJ, Yang J, An XM, Ma GW (2011) Modelling rock fracturing and blast-induced rock mass failure via advanced discretisation within the discontinuous deformation analysis framework. *Comput Geotech* 38(1):40–49
- Ooi ET, Song CM, Tin-Loi F, Yang ZJ (2012) Polygon scaled boundary finite elements for crack propagation modelling. *Int J Numer Methods Eng* 91(3):319–342
- Park CH (2008) Coalescence of frictional fractures in rock materials. Purdue University, Dissertation

- Park CH, Bobet A (2009) Crack coalescence in specimens with open and closed flaws: a comparison. *Int J Rock Mech Min Sci* 46(5):819–829
- Prudencio M, Van Sint Jan M (2007) Strength and failure modes of rock mass models with non-persistent joints. *Int J Rock Mech Min Sci* 44(6):890–902
- Trädegård A, Nilsson F, Östlund S (1998) FEM-remeshing technique applied to crack growth problems. *Comput Methods Appl Mech Eng* 160(1–2):115–131
- Vesga LF, Vallejo LE, Lobo-Guerrero S (2008) DEM analysis of the crack propagation in brittle clays under uniaxial compression tests. *Int J Numer Anal Methods Geomech* 32(11):1405–1415
- Wang Y, Li X, Wu YF, Ben YX, Li DS, Hao JM, Zhang B (2014) Research on relationship between crack initiation stress level and brittleness indices for brittle rocks. *Chin J Rock Mech Eng* 33(2): 264–275 (in Chinese)
- Wong LNY, Einstein HH (2009) Crack coalescence in molded gypsum and Carrara marble: part 1. macroscopic observations and interpretation. *Rock Mech Rock Eng* 42(3):475–511
- Wong RHC, Chau KT, Tang CA, Lin P (2001) Analysis of crack coalescence in rock-like materials containing three flaws—part 1: experimental approach. *Int J Rock Mech Min Sci* 38(7):909–924
- Wong RHC, Tang CA, Chau KT, Lin P (2002) Splitting failure in brittle rocks containing pre-existing flaws under uniaxial compression. *Eng Fract Mech* 69(17):1853–1871
- Wu ZJ, Wong LNY (2012) Frictional crack initiation and propagation analysis using the numerical manifold method. *Comput Geotech* 39:38–53
- Wu ZJ, Wong LNY (2013) Modeling cracking behavior of rock mass containing inclusions using the enriched numerical manifold method. *Eng Geol* 162:1–13
- Yang SQ (2011) Crack coalescence behavior of brittle sandstone samples containing two coplanar fissures in the process of deformation failure. *Eng Fract Mech* 78(17):3059–3081
- Yang SQ, Huang YH, Jing HW, Liu XR (2014a) Discrete element modeling on fracture coalescence behavior of red sandstone containing two unparallel fissures under uniaxial compression. *Eng Geol* 178: 28–48
- Yang SQ, Jing HW (2011) Strength failure and crack coalescence behavior of brittle sandstone samples containing a single fissure under uniaxial compression. *Int J Fract* 168(2):227–250
- Yang SQ, Jing HW, Xu T (2014b) Mechanical behavior and failure analysis of brittle sandstone specimens containing combined flaws under uniaxial compression. *J Cent South Univ* 21(5):2059–2073
- Yin P, Wong RHC, Chau KT (2014) Coalescence of two parallel pre-existing surface cracks in granite. *Int J Rock Mech Min Sci* 68:66–84
- Zhang XP, Wong LNY (2012) Cracking processes in rock-like material containing a single flaw under uniaxial compression: a numerical study based on parallel bonded-particle model approach. *Rock Mech Rock Eng* 45(5):711–737
- Zhao ZY, Zhang Y, Bao HR (2011) Tunnel blasting simulations by the discontinuous deformation analysis. *Int J Comput Methods* 8(2): 277–292
- Zhao XD, Zhang HX, Zhu WC (2014) Fracture evolution around pre-existing cylindrical cavities in brittle rocks under uniaxial compression. *Trans Nonferrous Metals Soc China* 24(3):806–815